



HAL
open science

Seasonal and interannual variations in the propagation of photosynthetically available radiation through the Arctic atmosphere

J. Laliberté, S. Bélanger, M. Babin

► **To cite this version:**

J. Laliberté, S. Bélanger, M. Babin. Seasonal and interannual variations in the propagation of photosynthetically available radiation through the Arctic atmosphere. *Elementa: Science of the Anthropocene*, 2021, 9 (1), 10.1525/elementa.2020.00083 . hal-03458191

HAL Id: hal-03458191

<https://hal.science/hal-03458191>

Submitted on 8 Apr 2022

HAL is a multi-disciplinary open access archive for the deposit and dissemination of scientific research documents, whether they are published or not. The documents may come from teaching and research institutions in France or abroad, or from public or private research centers.

L'archive ouverte pluridisciplinaire **HAL**, est destinée au dépôt et à la diffusion de documents scientifiques de niveau recherche, publiés ou non, émanant des établissements d'enseignement et de recherche français ou étrangers, des laboratoires publics ou privés.



Distributed under a Creative Commons Attribution 4.0 International License

RESEARCH ARTICLE

Seasonal and interannual variations in the propagation of photosynthetically available radiation through the Arctic atmosphere

J. Laliberté^{1,*}, S. Bélanger², and M. Babin¹

The Arctic atmosphere–surface system transmits visible light from the Sun to the ocean, determining the annual cycle of light available to microalgae. This light is referred to as photosynthetically available radiation (PAR). A known consequence of Arctic warming is the change at the atmosphere–ocean interface (longer ice-free season, younger ice), implying an increase in the percentage of PAR being transferred to the water. However, much less is known about the recent changes in how much PAR is being transferred by the overlying atmosphere. We studied the transfer of PAR through the atmosphere between May 21 and July 23 at a pan-Arctic scale for the period ranging from 2000 to 2016. By combining a large data set of atmospheric and surface conditions into a radiative transfer model, we computed the percentage of PAR transferred to the surface. We found that typical Arctic atmospheres convey between 60% and 70% of the incident PAR received from the Sun, meaning the Arctic atmosphere typically transmits more light than most sea ice surfaces, with the exception of mature melt ponds. We also found that the transfer of PAR through the atmosphere decreased at a rate of 2.3% per decade over the studied period, due to the increase in cloudiness and the weaker radiative interaction between the atmosphere and the surface. Further investigation is required to address how, in the warmer Arctic climate, this negative trend would compensate for the increased surface transmittance and its consequences on marine productivity.

Keywords: Arctic Ocean, Atmosphere, Surface, Clouds, Sea ice, Photosynthetically available radiation

1. Introduction

Earth's obliquity gives rise to large seasonal variations in the input of solar irradiance to Arctic marine ecosystems. Notably, it limits primary productivity during several months of the year, particularly during the polar night. During other times of the year, sea ice (including overlying snow) is what most constrains the amount of solar irradiance used by algae, named photosynthetically available radiation (PAR), in the water column. The impacts of ongoing climate-related changes on sea ice transparency to PAR have been emphasized in several recent studies (e.g., Arrigo et al., 2012; Assmy et al., 2017; Horvat et al., 2017). Significant reduction in the transfer of PAR through the atmosphere has also been observed at the pan-Arctic scale, impacting the marine primary production (Bélanger et al., 2013). PAR estimations at the sea surface by Bélanger et al. (2013), however, ignored the radiative interaction (i.e.,

multiple back and forth diffuse reflections) between the atmosphere and the highly reflective surface in the presence of sea ice. Laliberté et al. (2016) included this interaction in their PAR model and, based on in situ observations, showed its significance. Here, we further examined the variations in the propagation of PAR through the atmosphere over the Arctic Ocean while taking into account the interactions between the atmosphere and surface. We focus on the spring-to-summer transition when the solar irradiance is highest and both the ocean surface and the atmosphere change rapidly due to rising air temperature and melting snow and sea ice.

In this study, the surface is a horizontal layer that includes only the air–ocean interface for open waters and that extends enough vertically to encompass sea ice when it is present (including the air–ice and ice–ocean interfaces). Following this definition, we define the surface transmittance for PAR, T_s (%), as the ratio of downward irradiance integrated over the PAR spectral range (400–700 nm) in the water just below the sea surface or the bottom of the ice, $E_d(\text{PAR}, 0^-)$ (moles photons $\text{m}^{-2} \text{d}^{-1}$), and downward irradiance in the air just above the sea surface or the top of the ice, $E_d(\text{PAR}, 0^+)$ (moles photons $\text{m}^{-2} \text{d}^{-1}$):

$$T_s = \frac{E_d(\text{PAR}, 0^-)}{E_d(\text{PAR}, 0^+)} \times 100. \quad (1)$$

¹ Takuvik International Research Laboratory, Université Laval (Canada) & CNRS (France), Département de Biologie, Université Laval, Québec, Québec, Canada

² Département de Biologie, Chimie et Géographie, Groupes BORÉAS and Québec-Océan, Université du Québec à Rimouski, Rimouski, Québec, Canada

* Corresponding author:
Email: julien.laliberte@gmail.com

Accordingly, the percentage of PAR transferred through the atmosphere, T_a (%), is defined as the ratio between $E_d(\text{PAR}, 0^+)$ and downward irradiance at the top-of-the-atmosphere, $E_d(\text{PAR}, \text{TOA})$ (moles photons $\text{m}^{-2} \text{d}^{-1}$):

$$T_a = \frac{E_d(\text{PAR}, 0^+)}{E_d(\text{PAR}, \text{TOA})} \times 100. \quad (2)$$

Equation 2 presents the downward irradiance at the surface normalized by its top-of-the-atmosphere value. Note that T_a , just like T_s , could be seen as the “atmospheric transmittance,” except that it is significantly impacted by the boundary conditions. In other words, the radiative properties of the bottom layer at the base of the atmosphere are much more variable than those for T_s and can influence the amount of light available at the surface. For this reason, we will refer to the “percentage of PAR transferred through the atmosphere” or “normalized downwelling irradiance” rather than “atmospheric transmittance” to avoid confusion with the latter concept. Finally, in the chosen framework, $E_d(\text{PAR}, 0^-)$ is available to Arctic marine primary producers and results from $E_d(\text{PAR}, \text{TOA})$ and the balance of T_s and T_a (Bélanger et al., 2013):

$$E_d(\text{PAR}, 0^-) = E_d(\text{PAR}, \text{TOA}) \times T_s \times T_a. \quad (3)$$

T_s variations in the Arctic Ocean are mostly driven by changes in sea ice concentration and physical properties, including thickness, brine and air content, presence of melt water, and the state of the snow cover (Perovich, 2005; Arndt and Nicolaus, 2014). Because of their effect on $E_d(\text{PAR}, 0^+)$, the most critical factors controlling variations in T_a are cloudiness (Rabette and Pilewskie, 2002; Bélanger et al., 2013) and surface albedo (Grenfell and Perovich, 2004).

Sea ice cover and thickness are decreasing (Haas et al., 2008; Stroeve et al., 2012), while the older ice is replaced by more dynamic (more leads) and younger ice (larger melt pond coverage; Comiso, 2012; Nicolaus et al., 2012; Wang et al., 2016), resulting in an increase of T_s . In parallel, a general increase in cloudiness (Eastman and Warren, 2010) is especially noticeable in the spring and summer (Wang and Key, 2003), resulting in a decrease in T_a . This work focuses on evaluating the transfer of visible radiation in the atmosphere, T_a , and its change in space and time over the Arctic Ocean. We decomposed the Arctic Ocean into three regions, defined by their ice cover, and the marine productive season into four periods of the year, relevant to the spring bloom and centered on the summer solstice. Using satellite remote sensing data from multiple sources combined into a radiative transfer model, we computed T_a over 17 years for each region and period of the year. Interannual and seasonal trends are calculated and interpreted. Finally, we verify how T_a compares in magnitude to values of T_s .

2. Materials and methods

2.1. Model

$E_d(\text{PAR}, 0^+)$ and $E_d(\text{PAR}, \text{TOA})$ were computed every day between May 21 and July 23 for every $1^\circ \times 1^\circ$ pixel above the Arctic circle (66°N) for nonland areas between 2000

and 2016, resulting in $8,640 \text{ pixels} \times 64 \text{ days} \times 2$ estimates per year.

To compute the propagation of PAR through the Arctic atmosphere, we used the Santa Barbara Discrete ordinate Atmospheric Radiative Transfer (SBDART) computer program (Ricchiuzzi et al., 1998), a one-dimensional atmospheric radiative transfer model. The input variables were cloud fraction, cloud optical thickness, cloud top height, water vapor amount, total ozone amount, aerosol optical depth (AOD), and the surface albedo (see below). SBDART has been used extensively to propagate irradiance through the atmosphere (e.g., Shupe and Intrieri, 2004; Su et al., 2007; Grenfell and Perovich, 2008; Painter et al., 2012). For each pixel, two SBDART runs were made every day, one for the clear part of the sky, the other for the cloudy part. They were then blended conservatively according to the cloud fraction. Each run yielded spectrally resolved downward irradiance at a 3-nm spectral resolution and expressed in $\text{W m}^{-2} \mu\text{m}^{-1}$. The instantaneous estimates were then converted into daily values, assuming constant atmospheric and surface conditions throughout the day for the temporal integration (Frouin et al., 2003). Spectral results were integrated over the 400–700 nm band to achieve PAR estimates.

2.2. Inputs

All inputs from satellite data discussed in this section are summarized in **Table 1**, where the products, associated references, spatial/temporal resolutions, time span, and website of the satellite-derived inputs used to compute the above surface downward planar irradiance are presented.

An atmospheric data set was built from the Moderate Resolution Imaging Spectroradiometer (MODIS) Level 3 Atmosphere Gridded Product (MOD08 and MYD08; Platnick et al., 2017), which contains the diurnal (daytime) cloud fraction, cloud optical thickness, cloud top height, water vapor and ozone content, and AOD (10.5067/MODIS/MYD06_L2.006, 10.5067/MODIS/MOD06_L2.006). These atmospheric properties were retrieved from multiple observations collected during different times of the day and averaged on an equal-angle global grid (Hubanks et al., 2019). We downloaded data from both Terra and Aqua platforms and averaged them to obtain daily fields on a pixel basis.

We generated a surface albedo following a large-scale generic model of the seasonal evolution of albedo for the visible spectral range, modified from Perovich and Polashenski (2012) and Perovich et al. (2011; see also Perovich et al., 2002; Perovich et al., 2007; Light et al., 2015a). The visible sea ice albedo values were approximated from the spectral albedo measurements of Perovich (1996) and Light et al. (2008, 2015b). This empirical model distinguishes six transitions in the state of sea ice during a year (**Figure 1**). It takes into account the sea ice age, sea ice concentration, and a number of melting or freezing phases that are detected from space using passive microwaves. The phases were determined from the dates corresponding to early melt onset, melt onset, early freeze onset, and freeze onset (Markus et al., 2009). These onsets are based on surface dielectric properties changes,

Table 1. Satellite products used to derive $E_d(\text{PAR}, 0^+)$. DOI: <https://doi.org/10.1525/elementa.2020.00083.t1>

Product	Reference	Spatial, Temporal		
		Resolutions	Time Span	Website
MODIS atmosphere products (Aqua and Terra)	Platnick et al. (2017)	1° × 1°, daily	2000–2018	https://modis.gsfc.nasa.gov/data/dataproduct/mod08.php
Sea ice age	Tschudi et al. (2016)	25 × 25 km, weekly	1984–2016	https://nsidc.org/data/nsidc-0611
Sea ice concentration	Cavalieri et al. (1996)	25 × 25 km, daily	1979–2017	https://nsidc.org/data/nsidc-0051
Early melt onset, melt onset, early freeze onset, and freeze onset	Markus et al. (2009)	25 × 25 km, yearly	1979–2017	https://neptune.gsfc.nasa.gov/csb/

MODIS = Moderate Resolution Imaging Spectroradiometer.

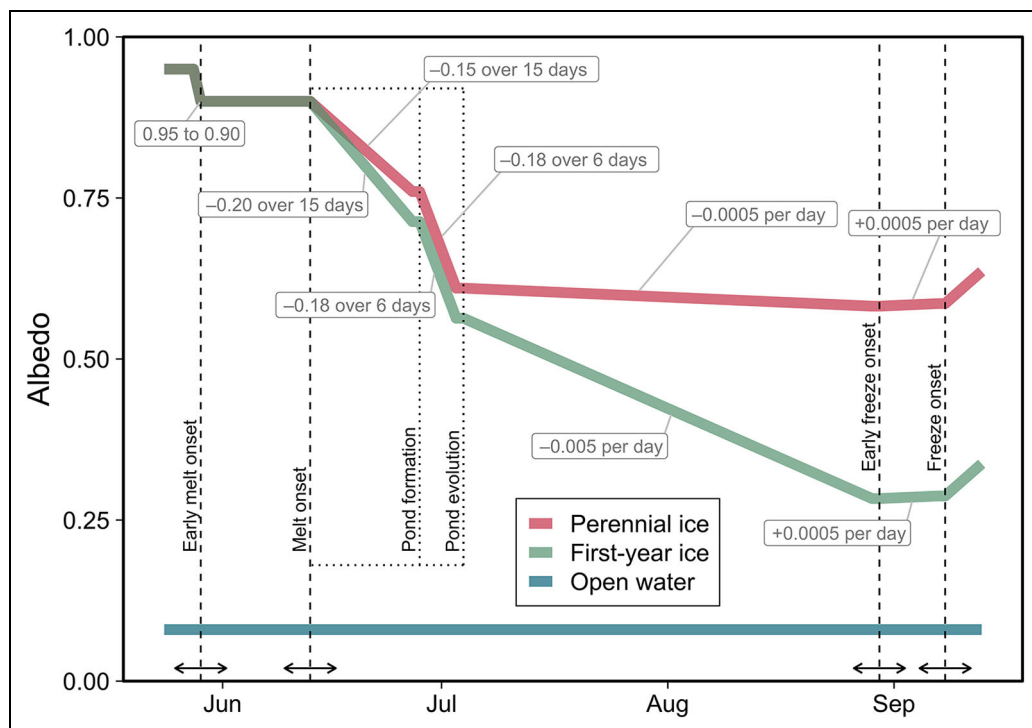


Figure 1. Schematic view of the empirical model to obtain the surface visible albedo. A typical evolution of the first-year (green line) and perennial ice albedo (red line) is shown. Both are combined with the open water albedo (blue line) according to sea ice concentration. The timing of the transitions is determined by the early melt onset, melt onset, early freeze onset, and freeze onset dates, with pond formation and pond evolution as additional transitions based on a constant time offset from the melt onset date. DOI: <https://doi.org/10.1525/elementa.2020.00083.f1>

monitored using the microwave signature of the surface. After winter, the early melt onset is the date when the sea ice surface layer emissivity first increases sharply due to the change in volumetric moisture content. The surface layer then undergoes melt-freeze cycles for some time, but eventually reaches the melt onset, a state when sea ice persistently stays under melt conditions, with signature approaching that of a blackbody in the microwave domain. The two other markers, the early freeze onset and freeze onset go in the opposite direction. The early freeze onset date is determined by the microwave signature showing evidence that the surface is starting to refreeze, and then freeze onset date is determined when the surface emissivity expresses persistent cold winter conditions.

The surface albedo was determined assuming specific sea ice albedo for each phase. When a pixel was ice-covered, its albedo progressed following a first-year ice (sea ice age indicating that it has not survived a melt period) or perennial ice scenario (sea ice age indicating it has survived a melt period; Tschudi et al., 2016). Although determining whether a parcel of first-year ice that has not survived a melt period was going to disappear over the summer was not possible, this unknown had little impact once albedo was combined with the sea ice concentration and melt/freeze indicators (Perovich et al., 2011). For both scenarios, a high stable albedo represented the cold winter phase. The first transition was triggered when the early melt onset date occurred, leading to

a small albedo decrease in the PAR spectral range. Then, after the melt onset was detected, a slow linear decrease was applied over 15 days to reproduce the snowmelt period. After that, a faster albedo linear decrease was used over a shorter period of 6 days to represent the melt pond formation. Subsequently, we represented the pond evolution by a small and constant decrease in the albedo, lasting until the arrival of the early freeze onset. The albedo increased slowly after the early freeze onset and faster after the freeze onset date, leveling at its initial winter value. At last, the surface albedo (A_s) varied as a function of time and was a weighted mean of the fraction of sea ice and open waters (Cavaleri et al., 1996) with a variable sea ice albedo (A_i) and a constant water albedo (A_w) of 0.08 (roughly representative of sun at 60° zenith angle under a clear sky). Accordingly, we have

$$A_s = A_i \times \text{SIC} + A_w \times (1 - \text{SIC}), \quad (4)$$

where the sea ice albedo is allowed to vary with time. When the sea ice concentration was available, but the early melt onset, melt onset, early freeze onset, or freeze onset were not, A_s was computed using an A_i of 0.40. This situation happened mainly in regions with low ice concentration, where we expect the existing ice to be free of snow.

We did not compute $E_d(\text{PAR}, 0^+)$ when cloud fraction, cloud optical thickness, or surface albedo were not available, which generally occurred over land-dominated pixels or near the North Pole where satellite orbit inclination limits data availability. When cloud fraction, cloud optical thickness and surface albedo were available, but cloud top height, ozone, water vapor content or AOD were not, missing values of the latter were replaced by climatological values, as these geophysical variables are not the main drivers of variations in $E_d(\text{PAR}, 0^+)$ in the Arctic (Barrientos Velasco et al., 2020). We calculated the daily climatology on a pixel basis from all available values over the 17-year MODIS data set. In the case of aerosol optical thickness, data were usually only available in summer because the presence of clouds and sea ice at other times prevented its retrieval (Tomasì et al., 2015). If satellite retrievals and even climatological values were nonexistent, we filled the gaps on the basis that AOD was 0.15 at the beginning of May and assumed to decrease linearly to 0.09 at the end of July (Tomasì et al., 2007; Breider et al., 2014). Finally, passive sensors do not allow to characterize the vertical distribution of clouds, but we found that changing the altitude of a given cloud deck in radiative transfer simulations generally resulted in $E_d(\text{PAR}, 0^+)$ changes of small magnitude (below 3%).

2.3. Comparison with a standard algorithm

Comparing the resulting $E_d(\text{PAR}, 0^+)$ product with near contemporaneous in situ measurement would not provide much insight because of the unknown subpixel spatial heterogeneity and the large spatial extent of the product. Comparing our product with other existing reanalysis products would also be difficult because of the lack of operational $E_d(\text{PAR}, 0^+)$ products. Besides, readily available surface radiative flux products (e.g., Extended AVHRR Polar Pathfinder data set; Key et al., 2016) are broadband,

and their conversion to a PAR range is highly dependent on atmospheric conditions and solar elevation (e.g., Frouin and Pinker, 1995). However, an operational $E_d(\text{PAR}, 0^+)$ algorithm used for primary production assessment exists and was compared with our product for its evaluation. We compared the $E_d(\text{PAR}, 0^+)$ obtained with our method (hereafter referred to as SBDART) to the standard $E_d(\text{PAR}, 0^+)$ product of the NASA Ocean Biology Processing Group (OBPG; Frouin et al., 2003), which has been successfully evaluated in the Arctic (Laliberté et al., 2016). The OBPG algorithm computes $E_d(\text{PAR}, 0^+)$ based on an energy budget approach, assuming that clouds are decoupled from the atmosphere and that the photons that are neither absorbed nor scattered out of the atmosphere reach the ocean. The OBPG $E_d(\text{PAR}, 0^+)$ product is currently limited to open waters because this approach does not address (1) the losses of photons due to absorption in sea ice, (2) the strong coupling between the surface and atmosphere over sea ice, and (3) the surface reflectance anisotropy of the changing sea ice surface (see Laliberté et al., 2016). Here, the OBPG $E_d(\text{PAR}, 0^+)$ product was downloaded for both Terra and Aqua and subsequently averaged. All data from the two methods were matched temporally and compared on a pixel-by-pixel basis. We computed linear Type II regression major axis using the R package `lmodel2` (Legendre, 2018) along with Pearson's correlation coefficient and the root-mean-square difference (RMSD):

$$\text{RMSD} = \sqrt{\frac{1}{N} \sum_{i=1}^N (\text{SBDART PAR}_i - \text{OBPG PAR}_i)^2}. \quad (5)$$

2.4. Analysis

To assess the changes in Arctic T_a when substantial marine primary production is expected (Ardyna et al., 2013), we divided the Arctic Ocean into three regions and four periods. The regions were defined as a function of their ice regime above 66° of latitude. This approach is justified by the coupling between the surface type cover and the atmospheric properties (Yu et al., 2019). Following Yu et al. (2019), the permanent ocean region was associated with all grid elements for which the sea ice concentration was consistently below 15% over 99% of all four periods considered for this study. In contrast, the permanent ice region was associated with all grid elements for which the sea ice concentration was above 15% over 99% of the time. The transient ice region was set to all grid elements not falling in the previous two categories. The permanent ocean region consisted mostly of the Greenland, Norwegian, and Barents seas. The transient ice included the Kara, Laptev, and East Siberian seas, as well as the Chukchi and Beaufort seas and Baffin Bay. The permanent ice region covered the Central Arctic Ocean and extends toward the West, as well as through the Canadian Archipelago. This division of the three regions is presented in **Figure 2**. Temporally, the productive period was divided into spring, late spring, early summer, and summer, each lasting 16 days (May 21 to June 5, June 6 to June 21, June 22 to July

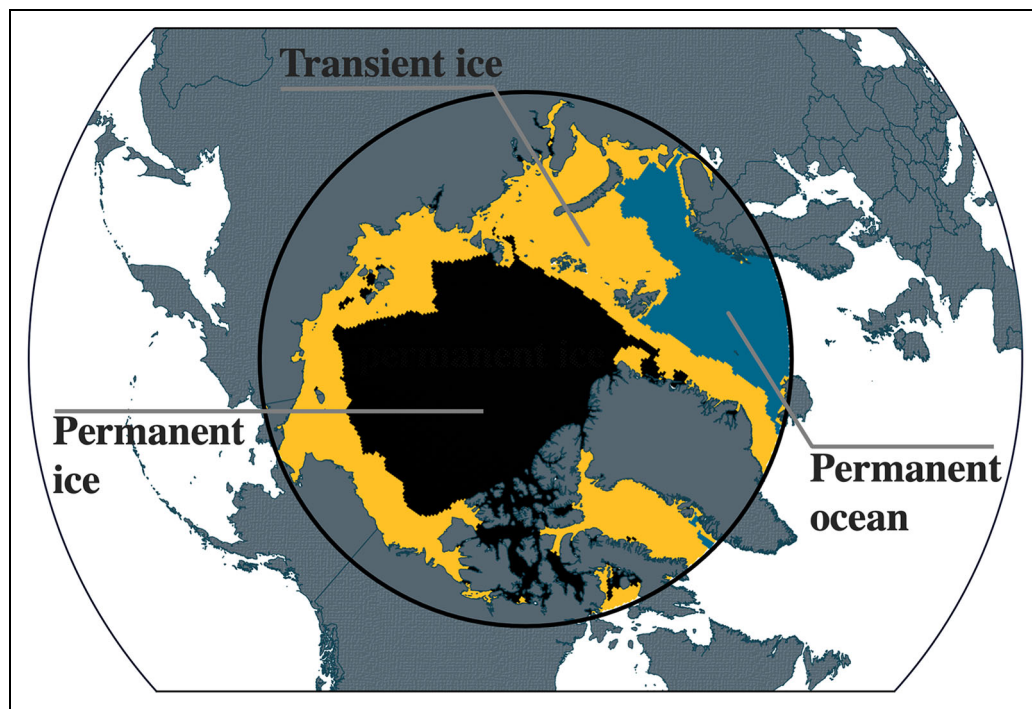


Figure 2. Map of the three Arctic regions. The permanent ocean region (blue) is defined as having a sea ice concentration that was steadily below 15% between May 21 and July 23 over the years 2000–2016. Similarly, the permanent ice region is defined as having a sea ice concentration above 15% for all of those same periods. The transient ice region is the remaining sector. DOI: <https://doi.org/10.1525/elementa.2020.00083.f2>

7, and July 8 to July 23). By doing so, we covered the timing when the maximum ice-covered and ice-free Arctic primary production is expected.

We first examined the seasonal evolution of E_d (PAR, 0^+) and the time of year when it reached its maximum value. Because different pixels covered different effective sizes of the surface, we used the area-weighted operator to bin the variables. The area-weighted median of E_d (PAR, 0^+) seasonal time series were examined separately for each region and year. On the same time series, we also identified the day of annual maximum by applying a 7-day moving average. A longer window would have blurred the variability, and a shorter window was susceptible to establishing the maximum to short-lived events such as isolated clear-sky days. Because the evolution of E_d (PAR, 0^+) varies greatly due to the seasonal insolation cycle, we also looked at its normalized value (T_a ; Equation 2), allowing greater focus on the role of atmosphere and surface properties. Two aspects of T_a were studied: the seasonal cycle and the multiyear trend. We derived the seasonal evolution for each region by calculating the median T_a of area-weighted pixel value on each day of the year. The seasonal evolution was derived for each individual region over all years. We used the median to reduce the gap created by missing MODIS-Terra data in the second half of June 2001 (MODIS-Aqua was only launched the following year). This analysis allowed us to obtain an overview of the seasonal evolution of T_a . We derived the multiyear trend for each region and for each period of the year ($6 \times 4 = 24$ trends). The area-weighted median of each region period and each year was computed, and a linear least-squares regression

was fitted on the 24 multiyear trends from 2000 to 2016. This approach allowed us to verify if T_a had changed over recent times.

3. Results and discussion

3.1. Inputs

Figure 3 provides a general description of the seven geophysical variables used as input in the SBDART computer program to determine the percentage of PAR transferred through the atmosphere, T_a , over each of the 8,640 grid cells for 64 days each year between 2000 and 2016. The median, interquartile range, and 10th and 90th percentiles of the distributions were computed from the satellite-derived variables and the albedo model (for numerical values, see Table S1), and the retrievals contributing to a single MODIS daily average were binned from multiple overlapping orbits (Hubanks et al., 2019). Consequently, the values presented in Table S1 represent a large amount of data (and multiple environmental conditions) and can be considered as climatological values representative of the Arctic. Cloud fraction was generally high over the Arctic around the summer solstice, with a moderate cloud optical thickness and low cloud altitudes, reflecting the prevalence of low-level clouds (Shupe and Intrieri, 2004). There was a higher cloud fraction over open waters. Visible surface albedo was highly heterogeneous through space and time for the regions with sea ice and decreased with time of year. The Arctic atmosphere was generally dry, especially in spring, but became more humid as first-year sea ice melted and leads developed (Curry et al., 1996; Kay and Gettelman, 2009), or as temperature

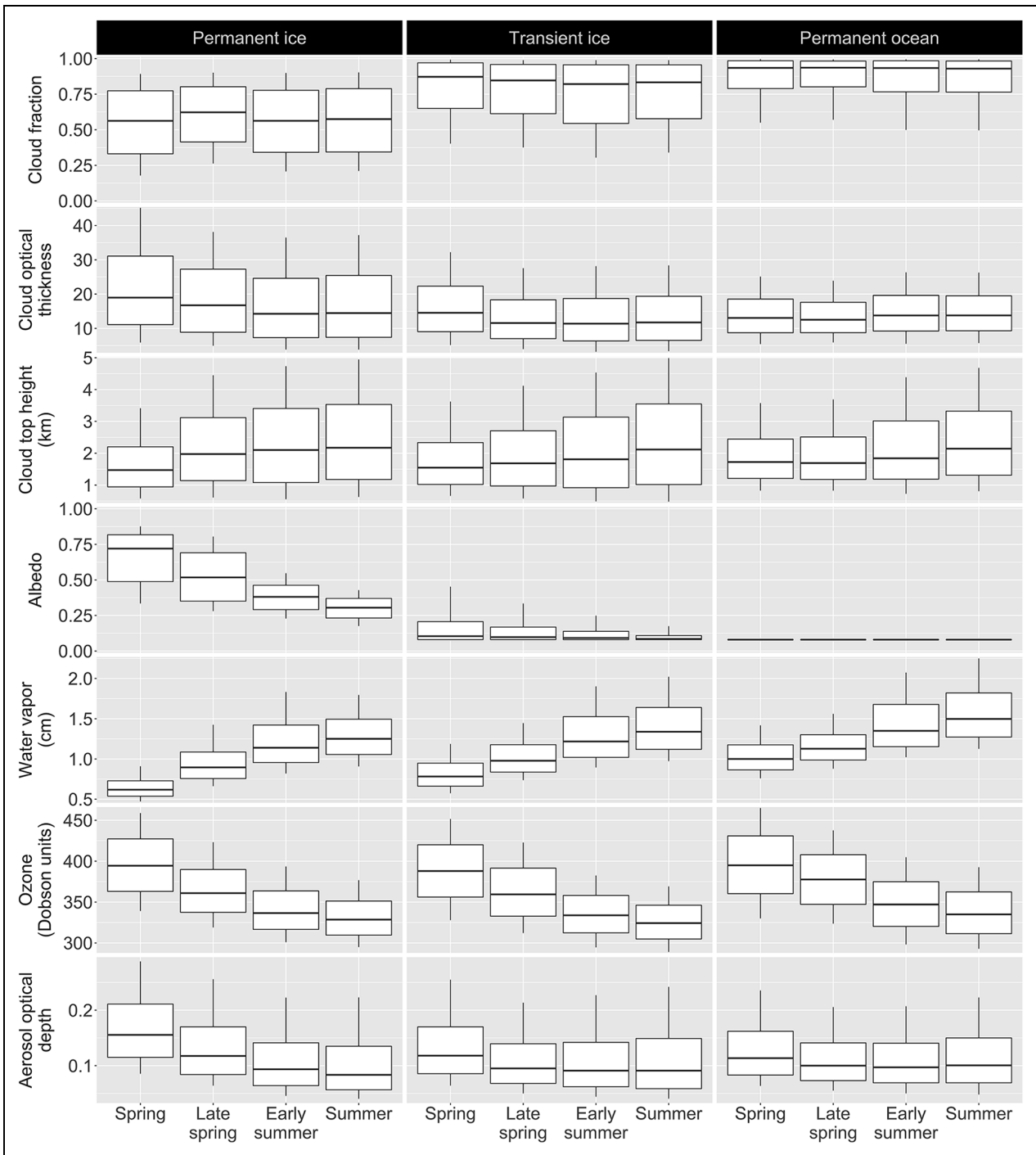


Figure 3. Values used as input for the radiative transfer simulations. For each of three defined regions and four periods, the different variables are represented with their median, interquartile range, and 10th and 90th percentiles of the distributions as the five features of the boxplots. DOI: <https://doi.org/10.1525/elementa.2020.00083.f3>

increased in the case of open waters. Regions with low albedo (consisting mainly of open waters; **Figure 2**) showed higher cloud fraction and humidity compared to where sea ice cover and land likely limited ocean evaporation. This result is consistent with the findings of Palm et al. (2010), who used satellite lidar measurements over the Arctic and found a higher cloud fraction over open waters than over sea ice. Although the ozone is known to exhibit a seasonal cycle of large amplitude over the Arctic, our study covered a time of year when this atmospheric gas

was near its annual mean value (approximately 380 DU; Fergusson, 2010) and slightly decreased with time of year for all three regions. For the studied period, 10% of the ozone and water vapor estimates were taken from our climatology (see Section 2.2). According to results presented in **Figure 3**, the classic atmosphere model for the subarctic summer from McClatchey et al. (1972) provides reasonable ozone content value (i.e., 350 DU) for the productive period but overestimates the atmospheric water vapor content (2.085 cm vs. approximately 1.0 cm). The

Arctic AOD median was 0.13, which is somewhat higher than when only valid retrievals from MODIS are considered (median of 0.10). The homogeneity of AOD values reported in Table S1 is due to the fact that 80% of the estimates were from the climatology. Fortunately, the above surface PAR is not sensitive to minor variations in AOD. For example, in Baffin Bay (74° , -74°) on June 1 under a clear sky or cloudy sky and wet snow on top of sea ice, reducing an AOD of 0.1 by 30% led to a reduction of above surface PAR of <1%.

3.2. Comparison with a standard algorithm

We compared the $E_d(\text{PAR}, 0^+)$ estimates obtained with the SBDART and OBPG methods. The latter was limited to open waters, defined as pixels having sea ice concentration lower than 10%. A total of 118,996 matching pixels yielded a regression slope of 0.72 and an intercept of 13.88 with a Pearson's correlation coefficient of 0.86 and an RMSD of $7.62 \text{ moles photons m}^{-2} \text{ d}^{-1}$ (Figure 4a).

In general, OBPG PAR estimates were higher than the SBDART estimates over open waters. The two methods employ largely different approaches, making a step-by-step comparison difficult. However, we speculate that our prescribed constant and conservative open water albedo value versus the estimate of the instantaneous surface albedo value in the OBPG method may cause a bias between methods. Frouin et al. (2018) used the aerosol and cloud properties from MERRA-2 hourly data to assess the OBPG algorithm uncertainties and also found that the OBPG method was slightly overestimating PAR. A weak overestimation by the OBPG algorithm was also observed when compared to in situ data collected shipboard from the Arctic (Laliberté et al., 2016) or from a moored buoy on the western side of Canada (Frouin et al., 2003). Nevertheless, the models are in good agreement, with a relatively low RMSD and a high correlation coefficient. Spatial patterns in OBPG and SBDART products (Figure 4b) are consistent, but a definitive advantage of using the SBDART method is that PAR can also be estimated in all sea ice conditions.

3.3. Seasonal evolution of $E_d(\text{PAR}, 0^+)$

The Arctic undergoes a strong seasonal cycle of $E_d(\text{PAR}, 0^+)$ due to the seasonal insolation cycle, with at least 1 day (summer solstice) when the sun is above the horizon for 24 h in the study period. Accordingly, the day of the summer solstice could be expected to be the day with the greatest incident irradiance, but in fact that is rarely the case. In this section, we examine the seasonal variations in $E_d(\text{PAR}, \text{TOA})$, $E_d(\text{PAR}, 0^+)$ under clear skies and actual sky conditions, and the distribution of dates for which $E_d(\text{PAR}, 0^+)$ reached its maximum every year (Figure 5).

As a reference, the $E_d(\text{PAR}, \text{TOA})$ peaked on the day of summer solstice and exhibited symmetrical decrease at decreasing and increasing days of the year (Figure 5). The $E_d(\text{PAR}, 0^+)$ calculated for a clear sky scenario also peaked on the day of summer solstice and showed a symmetrical distribution with time for the permanent ocean region where surface albedo was distinctively stable over all periods (Table S1). For the two other regions where the

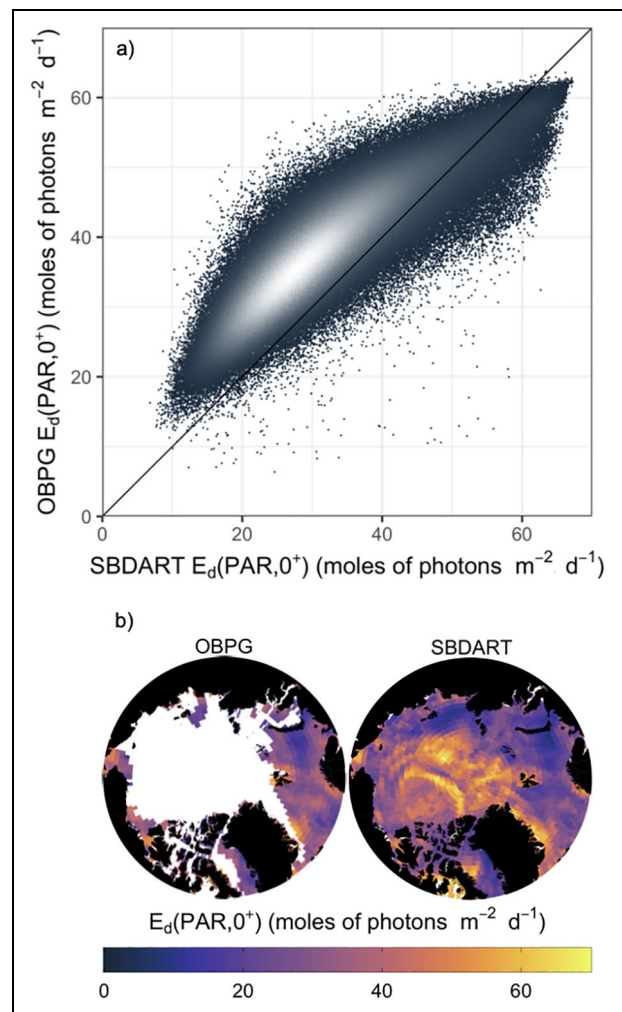


Figure 4. Comparison of $E_d(\text{PAR}, 0^+)$ from the SBDART and OBPG products. (a) Scatterplot showing the comparison between SBDART and OBPG products over the Arctic open ocean for the 2000–2016 period, with the solid black line as the 1-to-1 correspondence. (b) Example maps of both products for July 15, 2010. SBDART = Santa Barbara Discrete ordinate Atmospheric Radiative Transfer; OBPG = Ocean Biology Processing Group. DOI: <https://doi.org/10.1525/elementa.2020.00083.f4>

surface albedo experienced a considerable decrease between May 21 and July 23, the $E_d(\text{PAR}, 0^+)$ variation pattern under clear sky was slightly asymmetrical and peaked earlier (Figure 5), which suggests coupling between the atmosphere and the surface (Grenfell and Perovich, 2008). The $E_d(\text{PAR}, 0^+)$ calculated when accounting for actual sky conditions was strongly asymmetrical and peaked up to 4 weeks before the summer solstice. This early peaking is consistent with what was reported by Bernhard et al. (2007), who observed a day of annual maximum occurring 3 weeks before the summer solstice using their ground-based spectroradiometer located 300 m from the Chukchi Sea in Utqiagvik (Barrow), Alaska. Over the studied years, the transient ice region had the earliest day of annual maximum, with

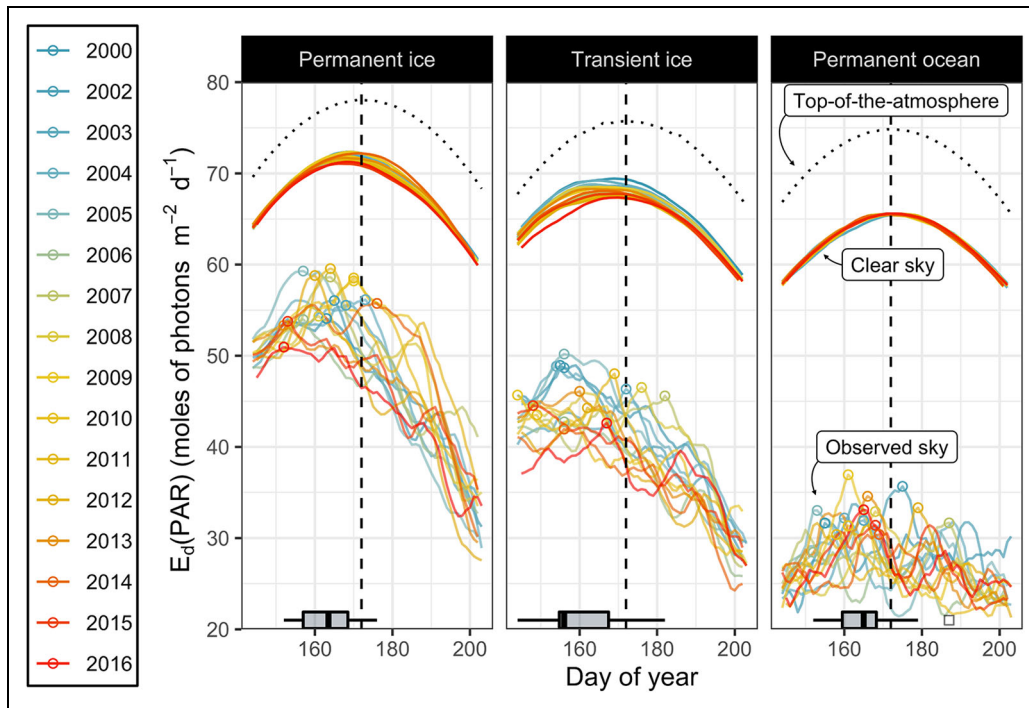


Figure 5. $E_d(\text{PAR})$ time series for each of three defined regions. The incident irradiance at the top-of-the-atmosphere and under clear and observed skies for the three defined Arctic regions over a 15-year period (2001 is absent because of a gap in the data) after a moving median with a window of 7 days was applied to the time series. The colored dots represent the day of annual maximum for each time series of $E_d(\text{PAR}, 0^+)$. At the bottom, the boxplots compile the distribution of the day of annual maximum, with the beginning and end of the gray boxes showing the interquartile range. The vertical dashed black line is the date of the summer solstice. DOI: <https://doi.org/10.1525/elementa.2020.00083.f5>

a median of 16 days before the summer solstice. The region with the latest annual $E_d(\text{PAR}, 0^+)$ maximum was the permanent ocean region with a median value of 7 days before the summer solstice.

The intuitive notion that the date of the summer solstice corresponds to an annual maximum in $E_d(\text{PAR}, 0^+)$ is not accurate in the Arctic. In other words, the seasonal insolation cycle is indeed a central factor determining the maximum observed $E_d(\text{PAR}, 0^+)$, but the annual cycle of Arctic environmental factors as well as synoptic events also have a significant effect. In fact, regions with similar top-of-the-atmosphere incident solar irradiances (i.e., in **Figure 2**, permanent ocean and transient ice regions cover similar latitudes) exhibit very different $E_d(\text{PAR}, 0^+)$ values and great interannual variability (**Figure 5**). For the rest of this article, we normalized $E_d(\text{PAR}, 0^+)$ by $E_d(\text{PAR}, \text{TOA})$ to obtain the percentage of PAR transferred through the atmosphere (T_a ; Equation 2, also named normalized downwelling irradiance) and inquire further into this variability.

3.4. Seasonal evolution of T_a

Variations in T_a are expected to be much less dependent on the insolation than $E_d(\text{PAR}, 0^+)$. Nonetheless, there was a small, second-order, remaining dependency due to the more prevalent slant path of the incoming sunlight through the atmosphere away from the summer solstice. As we restricted our study to a brief period symmetrically

positioned on either side of the summer solstice, we made sure that only an increase in cloudiness, a decrease in surface albedo, or a combination of both, can cause a transition of large magnitude in T_a (Gardiner, 1987; Fitzpatrick et al., 2004; Taskjelle et al., 2017a). **Figure 6** shows the median seasonal evolution (2000–2016) of T_a found for every region. To explore the impact of clouds and sea ice on the propagation of PAR through the Arctic atmosphere, we computed T_a for two additional scenarios. Keeping everything else constant, we computed the seasonal evolution for T_a under clear skies (no clouds; T_a clear sky in **Figure 6**) and for open water conditions (no sea ice; T_a open ocean in **Figure 6**). In the figure, the lines appear rather smooth because of the spatial and temporal averaging, which blurs the day-to-day variability and emphasizes the bulk seasonal evolution of each region.

Relative to T_a (red line in **Figure 6**, T_a), when removing the clouds from the simulations (turquoise line in **Figure 6**, T_a clear sky), the percentage of PAR transferred through the atmosphere increased. The effect of clouds can be seen by the difference between the red line and the turquoise line in **Figure 6**. When sea ice is removed from the simulations (yellow line in **Figure 6**, T_a open ocean), the normalized downwelling irradiance decreased (except on the right panel where the median T_a is plotted over the median T_a open ocean). The effect of sea ice is the difference between the red line and the yellow line.

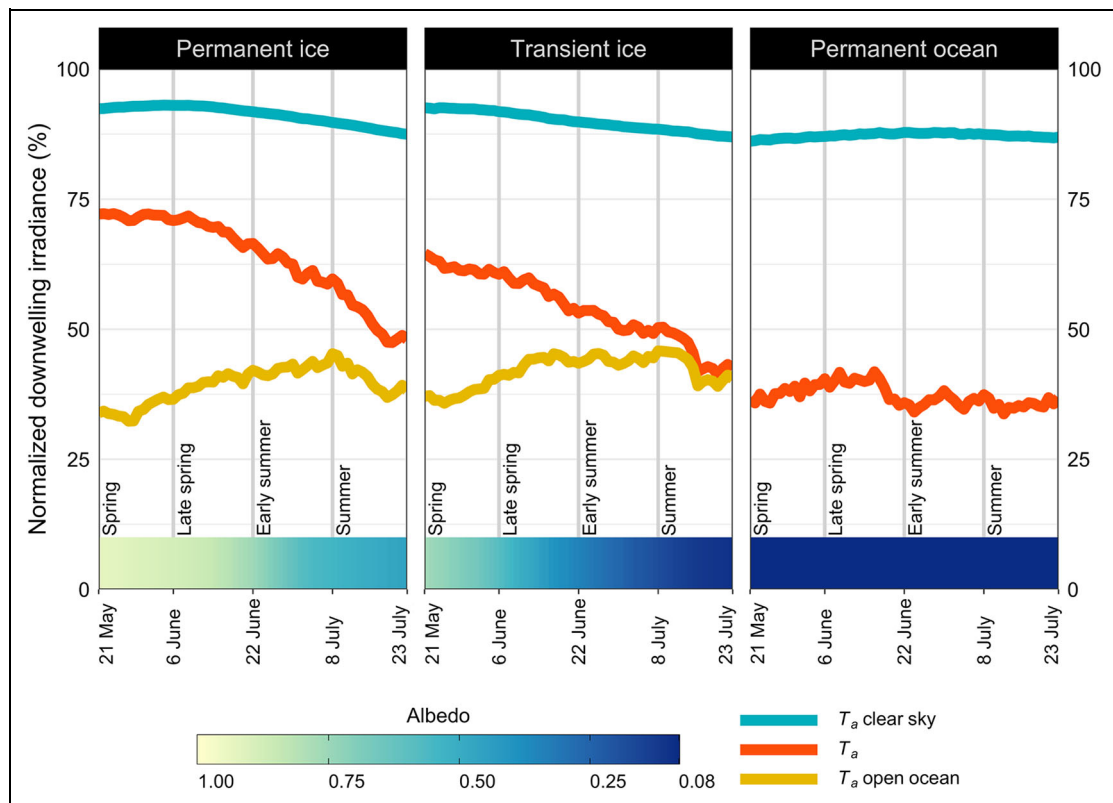


Figure 6. Median percentage of PAR transferred through the atmosphere. The percentage of PAR transferred through the atmosphere (T_a) for the years 2000–2016 as a function of the day of the year for each of the three defined Arctic regions is shown in red. The turquoise line at the top of the panels represents the percentage of PAR transferred through the atmosphere for the clear sky scenario (T_a clear sky), and the yellow line represents the percentage of PAR transferred through the atmosphere for the open water scenario (T_a open ocean). The bottom ribbon represents the median albedo. PAR = photosynthetically available radiation. DOI: <https://doi.org/10.1525/elementa.2020.00083.f6>

In all cases, the median percentage of PAR transferred through the atmosphere for the clear sky scenario remained above 85%, but always below 93%. This finding means that where the Arctic is cloud-free, we can expect that, in general, between 7% and 15% of E_d (PAR, TOA) would be lost through the cloudless atmosphere before reaching the surface. When averaged over the four periods, T_a clear sky was 91%, 90%, and 87% for the permanent ice, transient ice, and permanent ocean regions, respectively. When instead of removing clouds, we removed the sea ice (T_a open ocean), the normalized downwelling irradiance was between 46% and 32%. When averaged over the four periods, we find T_a open ocean of 39%, 42%, and 37% for the permanent ice, transient ice, and permanent ocean regions, respectively. These results allow us to further explore the general impact of clouds. Considering the difference between T_a clear sky and T_a open ocean, we may conclude that clouds are responsible on average for half (52%, 48%, and 50% for the permanent ice, transient ice, and permanent ocean regions, respectively) of the reduction of PAR being transferred through the atmosphere. Because, in reality, the Arctic surface is generally highly reflective, the normalized downwelling irradiance is higher than that. This fact is illustrated in both the regions of permanent ice and of transient ice, where early in the season (spring period), this reduction of normalized

downwelling irradiance (due to clouds, gases, and aerosols) was effectively cut by one-half and one-third, respectively, due to the presence of reflective sea ice. The surface, coupled to the overlying atmosphere, strongly affects the visible radiation available at the surface. This analysis reveals the sensitivity of the normalized downwelling irradiance to the parametrization of albedo and underlines the importance of having a proper surface albedo parametrization in the context of Arctic primary production modeling, especially when considering leads and the marginal ice zone (Bélanger et al., 2013; Blais et al., 2017).

3.5. Decadal trends in T_a

For this section, we focus on the interannual changes in T_a . **Figure 7** presents the trends in T_a from 2000 to 2016 separately for the three regions and four periods between May 21 and July 23. Overall, 10 of the 12 trends showed a decrease in T_a with time, including five that were statistically significant ($P < 0.05$).

As seen on **Figure 7**, the Arctic atmosphere, in general, shifted from relatively transparent to more opaque to PAR over the years. In the spring (May 21 to June 5), we found negative slopes for all three Arctic regions, with a mean of $-1.9\%/decade$ and a statistically significant slope for the transient ice regime ($P < 0.05$). Late spring was also characterized by negative T_a trends over all regions, with

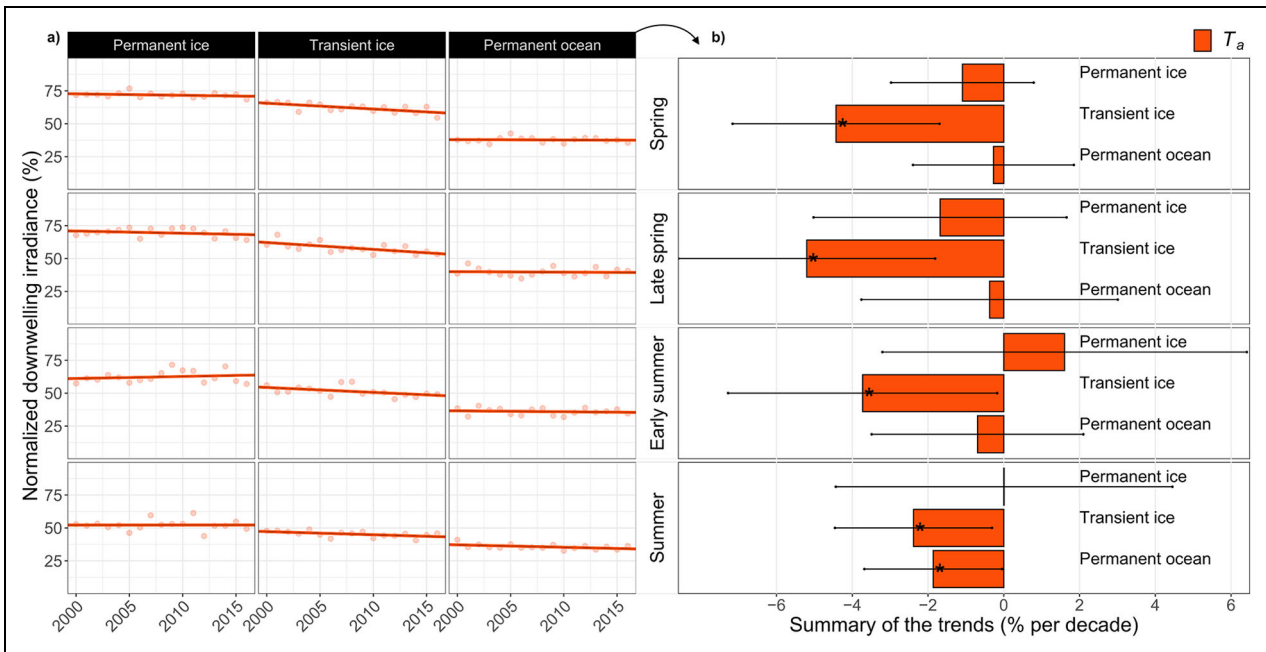


Figure 7. Trends in the percentage of PAR transferred through the atmosphere (T_a). Trends are presented over the years 2000–2016 for three Arctic regions and four periods, one per row (spring: May 21 to June 5, late spring: June 6 to June 21, early summer: June 22 to July 7, summer: July 8 to July 23), with (a) all of the annual median and overlaid linear regressions and (b) bar plots to emphasize quantitatively the slope sign and magnitude corresponding to the regressions in (a), with an asterisk to identify statistically significant slopes ($P < 0.05$). PAR = photosynthetically available radiation. DOI: <https://doi.org/10.1525/elementa.2020.00083.f7>

a mean of $-2.4\%/decade$ and significant slopes for the transient ice. Early summer and summer show weaker trends with means of $-0.9\%/decade$ and $-1.4\%/decade$, respectively. In summary, the permanent ice region displayed negative trends for the spring and late spring, but a positive trend in the early summer and no trend for the summer (none were significant). The transient ice region displayed negative and significant trends over all periods. In other words, the confidence intervals set at the conventional boundary suggest that there is a trend for the transient ice region over all periods. The permanent open ocean region showed negative trends for all periods, with the summer period as statistically significant, which, due to the definition of that region, points to an increase in cloudiness. Over the whole Arctic (considering all pixels weighted by their area), and for all considered periods (from May 21 to July 23), T_a decreased on average by $2.3\%/decade$ (statistically significant) between 2000 and 2016.

Since E_d (PAR, TOA) is stable over time, trends in E_d (PAR, 0^+) showed the same patterns as T_a . The overall decrease in E_d (PAR, 0^+) between 2000 and 2016 is consistent with the trends reported by Bélanger et al. (2013; their figure 1) for the 1998–2009 period. Interestingly, when computing the equivalent of **Figure 7** for the open ocean scenario (not shown), the trends were similar to those of T_a , but of weaker magnitude (average of $-0.54\%/decade$). Under this scenario, there is no ice, so the general decrease of the percentage of PAR being transferred by the atmosphere is most likely due to an increase in cloudiness over time. This explanation is consistent

with previous studies showing that water vapor content of the atmosphere (Rinke et al., 2019) and cloudiness (Liu et al., 2012) underwent long-term increases related to weaker and less persistent sea ice (Bintanja and Van Der Linden, 2013). For the clear sky scenario (not shown), the trends were of similar magnitude on average than those of the open ocean (average of $-0.59\%/decade$). Under this scenario, there are no clouds, meaning that part of the observed trends in the normalized downwelling irradiance can be ascribed to a reduction in surface albedo. Finally, the magnitude of the trends found for both extreme scenarios was not comparable to the observed trends in T_a . This discrepancy can be explained by the contribution of the surface–cloud interactions to the T_a trends. We speculate that an indirect consequence of the reduced interactions is causing a change in the spectral quality of the surface incident light over time, as these interactions increase the atmospheric pathlength and thus promotes molecular (Rayleigh) scattering of short wavelengths. This scattering effect could in turn impact the spectral shape of the marine light and therefore have consequences, although modest, on the fraction of PAR absorbed by microalgae.

3.6. Changes in T_a compared with possible changes in surface transmittance, T_s

Areal reduction of sea ice cover and changes in features of the ice pack (thickness, melt ponds, snow cover, ridging, and leads) have been at the forefront of recent Arctic research, notably because they affect the transmittance of the surface, T_s , and therefore the amount of light

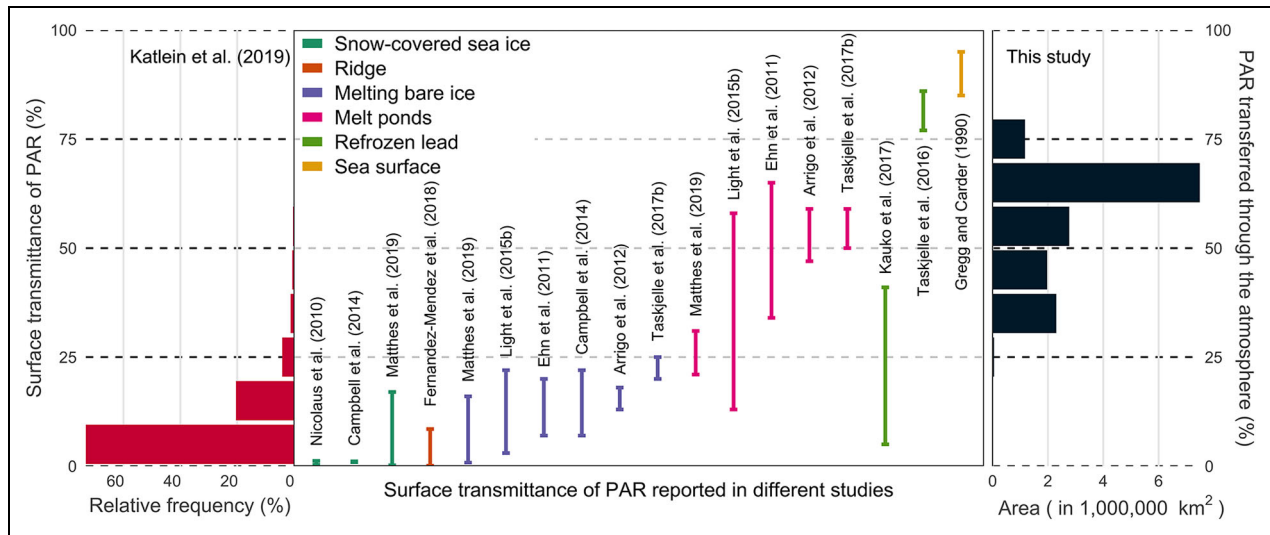


Figure 8. Comparison between PAR surface transmittance (T_s) and percentage of PAR transferred through the atmosphere (T_a). Sea ice transmittance values are computed from Katlein et al. (2019; left), in the context of different surface transmittances of PAR from previous studies (middle), along with the distribution of the percentage of PAR transferred through the atmosphere per surface area of the Arctic produced in this study (right). PAR = photosynthetically available radiation. DOI: <https://doi.org/10.1525/elementa.2020.00083.f8>

available for microalgae living in sea ice and the water column. That T_s is currently increasing in the Arctic is broadly recognized (Nicolaus et al., 2012; Slagstad et al., 2015; Tedesco et al., 2019). These changes in Arctic sea ice are thought to promote more frequent, massive under-ice phytoplankton blooms (Arrigo et al., 2012; Lowry et al., 2014; Assmy et al., 2017) and have been found to trigger earlier and more intense spring phytoplankton blooms (Kahru et al., 2016; Renault et al., 2018). Here, we have assessed that T_a decreased over the years for most regions and periods considered in this study. Unfortunately, we could not directly compare the magnitude of this decrease with the increase in T_s , because trends in T_s at a pan-Arctic scale are not yet available due in part to the difficulty of deriving physical and/or optical properties of snow and sea ice with good accuracy using remote sensing.

To provide a context for the reduction of T_a , however, we compiled in situ measurements of T_s found in the literature (Figure 8), and the sea surface transmittance for open waters from the model of Gregg and Carder (1990). In summary, for the three main Arctic surface types, namely, snow, bare ice, and melt ponds, T_s ranges from 0.2% to 17%, 0.8% to 25%, and 13% to 65%, respectively. Different authors also reported transmittance values for less commonly measured surface types, such as a sea ice ridge, having values ranging between 0.1% and 8.5%, and refrozen leads, having values ranging between 5% (including a snow cover) and 86%. These data are from first and multiyear ice and were collected over regions corresponding to Chukchi and Beaufort Seas, the Canadian Archipelago and Baffin Bay, the Greenland and Norwegian seas, and the Central Arctic Ocean. Additionally, Katlein et al. (2019) published a large collection of spectral values of sea ice transmittance acquired using a remotely operated vehicle, mostly in the Central Arctic Ocean (permanent sea ice). Over our studied period and spectral

range of interest, a distribution of their 19,815 T_s values is displayed (surface types were not specifically characterized) in Figure 8.

As shown in Figure 8, T_s ranges between less than 1% (snow-covered sea ice) and 95% (open waters, leads), with a mean for values from Katlein et al. (2019) below 10%. Across the Arctic, T_a has a mean of 60% with extremes of 25% and 75%. Light availability for under-ice phytoplankton is, broadly speaking (referring to the contrasting modes of the data distribution from Katlein et al., 2019, and present study distributions), dominated by the variations in T_s . In some places, however, where T_s is high, T_a could be the primary source of variations of PAR (open waters, refrozen leads, and sea ice with well-developed melt ponds).

During spring, a first drastic increase in T_s occurs when the snow starts to melt (the melt onset date generally occurs in early June), and a second drastic increase occurs when the melt ponds spread (a few weeks later in the melt season; Figure 1). Both are key transitions for microalgae (Palmer et al., 2014; Hancke et al., 2018). In the former, T_a is generally high (>70%; Figure 6) and likely plays a minor role, but in the latter, T_a is lower (45%–60%; Figure 6) and this decrease could partly compensate for the increase in T_s .

4. Conclusion

We gathered a large data set of atmospheric and surface Arctic conditions, which, when applied in radiative transfer simulations, allowed us to assess the variations in the percentage of PAR transferred through the atmosphere (also named normalized downwelling irradiance, T_a) at a pan-Arctic scale between the years 2000 and 2016. Our calculations showed that the maximum PAR available at the surface of the Arctic Ocean generally occurred up to 2 weeks before the summer solstice. In addition, we found

that every year, for the permanent ice and transient ice regions, the normalized downwelling irradiance decreased as the melt season progressed, mostly because of the decrease in surface albedo and the ensuing weaker radiative interaction with the overlying atmosphere. In the case of the permanent open ocean, clouds clearly showed an important impact on the visible light availability throughout the whole solar peak months. In fact, we determined that across the Arctic, if there were no sea ice, E_d (PAR, TOA) when propagated through the atmosphere would generally be reduced by 50% due only to the prevalent cloudiness (**Figure 6**). This strong impact is dampened by the radiative interaction between the clouds and the sea ice. Finally, we found that on average, the percentage of PAR transferred by the Arctic atmosphere decreased at a statistically significant rate of 2.3%/decade. The spatial domain with the largest negative trends in our normalized downwelling irradiance was the transient ice region. This change over the years probably altered the interaction between the surface and the atmosphere, perhaps modifying the spectral characteristics of marine light.

Most studies of the seasonal evolution of phytoplankton in the Arctic do not identify cloudiness as a determinant factor influencing the annual cycle of light. Although many have emphasized the influence of snow, melt ponds, leads, and ice thickness (Mundy et al., 2005; Arrigo et al., 2012; Assmy et al., 2017; Horvat et al., 2017), much less is known about the variations in the propagation of PAR through the Arctic atmosphere. Here, we found that between 60% and 70% of the top-of-the-atmosphere incident PAR typically reached the Arctic surface, whereas the surface transmittance (T_s) often ranged between 0% and 20%, except for melt ponds which increase T_s up to 65%, a value comparable in magnitude to the percentage of PAR being transferred by the atmosphere. Thus, a next step would be to use our framework (Equation 3) to monitor the relation between the atmospheric and surface optically active components (mainly water in diverse states) over a small area at high temporal resolution during the key transition period when E_d (PAR, 0⁻) increases rapidly due to melt pond formation. Because of the important impact of clouds on light availability, we speculate that on certain occasions, long-lasting clear sky events (which were not discernible with our coarser spatial resolution) could play a role in triggering the phytoplankton spring bloom.

Clouds influence sea ice (Kay et al., 2008; Kay and Gettelman, 2009; Huang et al., 2019; Choi et al., 2020), and sea ice exerts control on clouds (Wang and Key, 2003; Budikova, 2009; Sato et al., 2012; He et al., 2019). This complex feedback interaction is also found when considering their respective influence on the propagation of PAR through the large-scale Arctic atmosphere-ice-ocean system. Further investigation is required to address how, in the warmer Arctic climate, the negative trend in the percentage of PAR transferred through the atmosphere would compensate for the increased surface transmittance. Because both are evolving in opposite directions every season, and also over the years, retrieving T_s at the pan-Arctic scale would allow a characterization of the balance for these

changes. As a large part of the incident visible light is scattered upward after reaching sea ice, a robust satellite remote sensing method to derive sea ice visible albedo over the Arctic Ocean could help constrain T_s .

Data accessibility statement

All data from the model are publicly available at the polar data catalogue (https://www.polardata.ca/pdcsearch/PDCSearchDOI.jsp?doi_id=13179).

Supplemental file

The supplemental file for this article can be found as follows:

Table S1. Docx

Acknowledgment

We gratefully acknowledge scientific and financial support of Québec-Océan.

Funding

Julien Laliberté was funded by the FRQNT and the CREATE program (NSERC). Simon Bélanger was funded by NSERC (RGPIN-2019-06070). Marcel Babin was funded by NSERC (05175-2014). This work was funded by the Canadian Excellence Research Chair on Remote Sensing of Canada's new Arctic frontier, the Canadian Space Agency Green-Edge project, the CNES GreenEdge project (131425), and the Network of Centres of Excellence MEOPAR, Observation core in remote sensing project (1-02-01-064.5).

Competing interests

The authors declare that there is no conflict of interest and agree to submission at this time.

Author contributions

Designed and wrote the study: JL.

Contributed to its conception and edited this article: SB, MB.

Approved the submitted version for publication: All authors.

References

- Ardyna, M, Babin, M, Gosselin, M, Devred, E, Bélanger, S, Matsuoka, A, Tremblay, J-É.** 2013. Parameterization of vertical chlorophyll *a* in the Arctic Ocean: Impact of the subsurface chlorophyll maximum on regional, seasonal, and annual primary production estimates. *Biogeosciences* **10**(6): 4383–4404. DOI: <http://dx.doi.org/10.5194/bg-10-4383-2013>.
- Arndt, S, Nicolaus, M.** 2014. Seasonal cycle and long-term trend of solar energy fluxes through Arctic sea ice. *The Cryosphere* **8**(6): 2219–2233. DOI: <http://dx.doi.org/10.5194/tc-8-2219-2014>.
- Arrigo, KR, Perovich, DK, Pickart, RS, Brown, ZW, van Dijken, GL, Lowry, KE, Mills, MM, Palmer, MA, Balch, WM, Bahr, F, Bates, NR, Benitez-Nelson, C, Bowler, B, Brownlee, E, Ehn, JK, Frey, KE, Garley, R, Laney, SR., Lubelczyk, L, Mathis, J, Matsuoka, A, Mitchel, BG, Moore, G WK, Ortega-Retuerta, E, Pal, S, Polashenski, CM, Reynolds,**

- RA, Schieber, B, Sosik, HM, Stephens, M, Swift, JH.** 2012. Massive phytoplankton blooms under Arctic sea ice. *Science* **336**(6087): 1408. DOI: <http://dx.doi.org/10.1126/science.1215065>.
- Assmy, P, Fernández-Méndez, M, Duarte, P, Meyer, A, Randelhoff, A, Mundy, CJ, Olsen, LM, Kauko, HM, Bailey, A, Chierici, M, Cohen, L, Doulgeris, AP, Ehn, JK, Fransson, A, Gerland, S, Hop, H, Hudson, SR, Hugues, N, Itkin, P, Johnsen, G, King, JA, Koch, BP, Koenig, Z, Kwasniewski, S, Laney, SR, Nicolaus, M, Pavlov, AK, Polashenski, CM, Provost, C, Rösel, A, Sandbu, M, Spreen, G, Smedsrud, LH, Sundfjord, A, Taskjelle, T, Tatar-ek, A, Wiktor, J, Wagner, RM, Wold, A, Steen, H & Granskog, MA.** 2017. Leads in Arctic pack ice enable early phytoplankton blooms below snow-covered sea ice. *Scientific Reports* **7**: 40850. DOI: <http://dx.doi.org/10.1038/srep40850>.
- Barrientos Velasco, C, Deneke, H, Griesche, H, Seifert, P, Engelmann, R, Macke, A.** 2020. Spatiotemporal variability of solar radiation introduced by clouds over Arctic sea ice. *Atmospheric Measurement Techniques* **13**(4): 1757–1775. DOI: <http://dx.doi.org/10.5194/amt-13-1757-2020>.
- Bélanger, S, Babin, M, Tremblay, J-É.** 2013. Increasing cloudiness in Arctic damps the increase in phytoplankton primary production due to sea ice receding. *Biogeosciences* **10**(6): 4087–4101. DOI: <http://dx.doi.org/10.5194/bg-10-4087-2013>.
- Bernhard, G, Booth, CR, Ehramjian, JC, Stone, R, Dutton, EG.** 2007. Ultraviolet and visible radiation at Barrow, Alaska: Climatology and influencing factors on the basis of version 2 National Science Foundation network data. *Journal of Geophysical Research* **112**(D09101), 19p. DOI: <http://dx.doi.org/10.1029/2006jd007865>.
- Bintanja, R, van der Linden, EC.** 2013. The changing seasonal climate in the Arctic. *Scientific Reports* **3**: 1556. DOI: <http://dx.doi.org/10.1038/srep01556>.
- Blais, M, Ardyna, M, Gosselin, M, Dumont, D, Bélanger, S, Tremblay, JÉ, Gratton, Y, Marchese, C, Poulin, M.** 2017. Contrasting interannual changes in phytoplankton productivity and community structure in the coastal Canadian Arctic Ocean. *Limnology and Oceanography* **62**(6): 2480–2497. DOI: <https://doi.org/10.1002/lno.10581>.
- Breider, TJ, Mickley, LJ, Jacob, DJ, Wang, Q, Fisher, JA, Chang, RY-W, Alexander, B.** 2014. Annual distributions and sources of Arctic aerosol components, aerosol optical depth, and aerosol absorption. *Journal of Geophysical Research: Atmospheres* **119**(7): 4107–4124. DOI: <http://dx.doi.org/10.1002/2013jd020996>.
- Budikova, D.** 2009. Role of Arctic sea ice in global atmospheric circulation: A review. *Global and Planetary Change* **68**(3): 149–163. DOI: <https://doi.org/10.1016/j.gloplacha.2009.04.001>.
- Campbell, K, Mundy, CJ, Barber, DG, Gosselin, M.** 2014. Remote estimates of ice algae biomass and their response to environmental conditions during spring melt. *Arctic* **67**(3): 375–387. DOI: <http://dx.doi.org/10.14430/arctic4409>.
- Cavaliere, DJ, Parkinson, CL, Gloersen, P, Zwally, HJ.** 1996. Sea ice concentrations from Nimbus-7 SMMR and DMSP SSM/I-SSMIS Passive Microwave Data, Version 1, updated yearly, Boulder, Colorado USA. NASA National Snow and Ice Data Center Distributed Active Archive Center. DOI: <http://dx.doi.org/10.5067/8GQ8LZQVL0VL>.
- Choi, YS, Hwang, J, Ok, J, Park, DSR, Su, H, Jiang, JH, Huang, L, Limpasuvan, T.** 2020. Effect of Arctic clouds on the ice-albedo feedback in midsummer. *International Journal of Climatology* **40**(10): 4707–4714. DOI: <https://doi.org/10.1002/joc.6469>.
- Comiso, JC.** 2012. Large decadal decline of the Arctic multiyear ice cover. *Journal of Climate* **25**(4): 1176–1193. DOI: <http://dx.doi.org/10.1175/JCLI-D-11-00113.1>.
- Curry, JA, Rossow, WB, Randall, D, Schramm, JL.** 1996. Overview of Arctic cloud and radiation characteristics. *Journal of Climate* **9**: 1731–1764. DOI: [http://dx.doi.org/10.1175/1520-0442\(1996\)009<1731:OOACAR>2.0.CO;2](http://dx.doi.org/10.1175/1520-0442(1996)009<1731:OOACAR>2.0.CO;2).
- Eastman, R, Warren, SG.** 2010. Interannual variations of Arctic cloud types in relation to sea ice. *Journal of Climate* **23**(15): 4216–4232. DOI: <http://dx.doi.org/10.1175/2010JCLI3492.1>.
- Ehn, JK, Mundy, CJ, Barber, DG, Hop, H, Rossnagel, A, Stewart, J.** 2011. Impact of horizontal spreading on light propagation in melt pond covered seasonal sea ice in the Canadian Arctic. *Journal of Geophysical Research: Oceans* **116**: C00G02, 15 p. DOI: <http://dx.doi.org/10.1029/2010JC006908>.
- Fergusson, A.** 2010. The Arctic ozone layer: How the Arctic ozone layer is responding to ozone-depleting chemicals and climate change. *Environment Canada Report En164-18/2010E* **52**.
- Fernández-Méndez, M, Olsen, LM, Kauko, HM, Meyer, A, Rösel, A, Merkouriadi, I, Mundy, CJ, Ehn, JK, Johansson, AM, Wagner, PM, Ervik, Å, Sorrell, BK, Duarte, P, Wold, A, Hop, H, Assmy, P.** 2018. Algal hot spots in a changing Arctic Ocean: Sea-ice ridges and the snow-ice interface. *Frontiers in Marine Science* **5**. DOI: <http://dx.doi.org/10.3389/fmars.2018.00075>.
- Fitzpatrick, MF, Brandt, RE, Warren, SG.** 2004. Transmission of solar radiation by clouds over snow and ice surfaces: A parameterization in terms of optical depth, solar zenith angle, and surface albedo. *Journal of Climate* **17**: 266–275. DOI: [http://dx.doi.org/10.1175/1520-0442\(2004\)017<0266:TOSRBC>2.0.CO;2](http://dx.doi.org/10.1175/1520-0442(2004)017<0266:TOSRBC>2.0.CO;2).
- Frouin, R, Franz, BA, Werdell, PJ.** 2003. The SeaWIFS PAR product, in Hooker, SB, Firestone, ER eds., *Algorithm Updates for the Fourth SeaWIFS Data Reprocessing, NASA/TM 2003-206892*. Greenbelt, MD: NASA Goddard Space Flight Center: 46–50.
- Frouin, R, Pinker, RT.** 1995. Estimating photosynthetically active radiation (PAR) at the earth's surface from satellite observations. *Remote Sensing of*

- Environment* **51**(1): 98–107. DOI: [https://doi.org/10.1016/0034-4257\(94\)00068-X](https://doi.org/10.1016/0034-4257(94)00068-X).
- Frouin, R, Ramon, D, Jolivet, D, Compiègne, M.** 2018. Specifying algorithm uncertainties in satellite-derived PAR products. *Remote Sensing of the Open and Coastal Ocean and Inland Waters*, Vol. 10778. International Society for Optics and Photonics, 107780 W. DOI: <http://dx.doi.org/10.1117/12.2501681>.
- Gardiner, BG.** 1987. Solar radiation transmitted to the ground through cloud in relation to surface albedo. *Journal of Geophysical Research: Atmospheres* **92**(D4): 4010–4018. DOI: <http://dx.doi.org/10.1029/JD092iD04p04010>.
- Gregg, WW, Carder, KL.** 1990. A simple spectral solar irradiance model for cloudless maritime atmospheres. *Limnology and Oceanography* **35**(8): 1657–1675. DOI: <http://dx.doi.org/10.4319/lo.1990.35.8.1657>.
- Grenfell, TC, Perovich, DK.** 2004. Seasonal and spatial evolution of albedo in a snow-ice-land-ocean environment. *Journal of Geophysical Research* **109**: C01001. DOI: <http://dx.doi.org/10.1029/2003jc001866>.
- Grenfell, TC, Perovich, DK.** 2008. Incident spectral irradiance in the Arctic Basin during the summer and fall. *Journal of Geophysical Research: Atmospheres* **113**: D12117, 13. DOI: <http://dx.doi.org/10.1029/2007JD009418>.
- Haas, C, Pfaffling, A, Hendricks S, Rabenstein, L, Etienne, J L, Rigor, I.** 2008. Reduced ice thickness in Arctic transpolar drift favors rapid ice retreat. *Geophysical Research Letters* **35**: L17501. DOI: <http://dx.doi.org/10.1029/2008GL034457>.
- Hancke, K, Lund-Hansen, LC, Lamare, ML, Pederson, SH, King, MD, Andersen, P, Sorrell, BK.** 2018. Extreme low light requirement for algae growth underneath sea ice: A case study from Station Nord, NE Greenland. *Journal of Geophysical Research: Oceans* **123**(2): 985–1000. DOI: <http://dx.doi.org/10.1002/2017jc013263>.
- He, M, Hu, Y, Chen, N, Wang, D, Huang, J, Stamnes, K.** 2019. High cloud coverage over melted areas dominates the impact of clouds on the albedo feedback in the Arctic. *Scientific Reports* **9**(1): 1–11. DOI: <https://doi.org/10.1038/s41598-019-44155-w>.
- Horvat, C, Jones, DR, Iams, S, Schroeder, D, Flocco, D, Feltham, D.** 2017. The frequency and extent of sub-ice phytoplankton blooms in the Arctic Ocean. *Science Advances* **3**(3): e1601191. DOI: <http://dx.doi.org/10.1126/sciadv.1601191>.
- Huang, Y, Dong, X, Bailey, DA, Holland, MM, Xi, B, DuVivier, AK, Kay, J, Landrum, LL, Deng, Y.** 2019. Thicker clouds and accelerated Arctic sea ice decline: The atmosphere-sea ice interactions in spring. *Geophysical Research Letters* **46**(12): 6980–6989. DOI: <https://doi.org/10.1029/2019GL082791>.
- Hubanks, P, Platnick, S, King, M, Ridgway, B.** 2019. MODIS Atmosphere L3 Gridded Product Algorithm Theoretical Basis Document (ATBD) and Users Guide. *Collection 6.0 & 6.1, Version 4.4*, p. 124.
- Kahru, M, Lee, Z, Mitchell, BG, Nevison, CD.** 2016. Effects of sea ice cover on satellite-detected primary production in the Arctic Ocean. *Biological Letters* **12**(11): 20160223. DOI: <http://dx.doi.org/10.1098/rsbl.2016.0223>.
- Katlein, C, Arndt, S, Belter, HJ, Castellani, G, Nicolaus, M.** 2019. Seasonal evolution of light transmission distributions through Arctic sea ice. *Journal of Geophysical Research: Oceans* **124**(8): 5418–5435. DOI: <http://dx.doi.org/10.1029/2018jc014833>.
- Kauko, HM, Taskjelle, T, Assmy, P, Pavlov, AK, Mundy, CJ, Duarte, P, Fernández-Méndez, M, Olsen, LM, Hudson, SR, Johnsen, G, Elliott, A, Wang, F, Granskog, MA.** 2017. Windows in Arctic sea ice: Light transmission and ice algae in a refrozen lead. *Journal of Geophysical Research: Biogeosciences* **122**: 1486–1505. DOI: <http://dx.doi.org/10.1002/2016JG003626>.
- Kay, JE, Gettelman, A.** 2009. Cloud influence on and response to seasonal Arctic sea ice loss. *Journal of Geophysical Research* **114**: D18204. DOI: <http://dx.doi.org/10.1029/2009jd011773>.
- Kay, JE, L'Ecuyer, T, Gettelman, A, Stephens, G, O'Dell, C.** 2008. The contribution of cloud and radiation anomalies to the 2007 Arctic sea ice extent minimum. *Geophysical Research Letters* **35**(8). DOI: <https://doi.org/10.1029/2008GL033451>.
- Key, J, Wang, X, Liu, Y, Dworak, R, Letterly, A.** 2016. The AVHRR Polar Pathfinder Climate Data Records. *Remote Sensing* **8**(3): 167. DOI: <https://doi.org/10.3390/rs8030167>.
- Laliberté, J, Bélanger, S, Frouin, R.** 2016. Evaluation of satellite-based algorithms to estimate photosynthetically available radiation (PAR) reaching the ocean surface at high northern latitudes. *Remote Sensing of Environment* **184**: 199–211. DOI: <http://dx.doi.org/10.1016/j.rse.2016.06.014>.
- Legendre, P.** 2018. Model II Regression. *R package*. Available at <https://CRAN.R-project.org/package=lmodel2>. Accessed 1 August 2019.
- Light, B, Dickinson, S, Perovich, DK, Holland, MM.** 2015a. Evolution of summer Arctic sea ice albedo in CCSM4 simulations: Episodic summer snowfall and frozen summers. *Journal of Geophysical Research: Oceans* **120**(1), 284–303. DOI: <http://dx.doi.org/10.1002/2014jc010149>.
- Light, B, Grenfell, TC, Perovich, DK.** 2008. Transmission and absorption of solar radiation by Arctic sea ice during the melt season. *Journal of Geophysical Research: Oceans* **113**(C3): C03023. DOI: <http://dx.doi.org/10.1029/2006JC003977>.
- Light, B, Perovich, DK, Webster, MA, Polashenski, C, Dadic, R.** 2015b. Optical properties of melting first-year Arctic sea ice. *Journal of Geophysical Research: Oceans* **120**: 7657–7675. DOI: <http://dx.doi.org/10.1002/2015JC011163>.
- Liu, Y, Key, JR, Liu, Z, Wang, X, Vavrus, SJ.** 2012. A cloudier Arctic expected with diminishing sea ice.

- Geophysical Research Letters* **39**: L05705. DOI: <http://dx.doi.org/10.1029/2012gl051251>.
- Lowry, KE, van Dijken, GL, Arrigo, KR.** 2014. Evidence of under-ice phytoplankton blooms in the Chukchi Sea from 1998 to 2012. *Deep Sea Research Part II: Topical Studies in Oceanography* **105**: 105–117. DOI: <http://dx.doi.org/10.1016/j.dsr2.2014.03.013>.
- Markus, T, Stroeve, JC, Miller, J.** 2009. Recent changes in Arctic sea ice melt onset, freezeup, and melt season length. *Journal of Geophysical Research: Oceans* **114**: C12024. DOI: <http://dx.doi.org/10.1029/2009JC005436>.
- Matthes, LC, Ehn, JK, Lambert-Girard, S, Pogorzelec, NM, Babin, M, Mundy, CJ.** 2019. Average cosine coefficient and spectral distribution of the light field under sea ice: Implications for primary production. *Elementa Science of Anthropocene* **7**(1): 25. DOI: <http://dx.doi.org/10.1525/journal.elementa.363>.
- McClatchey, RA, Fenn, RW, Selby, JEA., Volz, FE, Garing, JS.** 1972. *Optical properties of the atmosphere*. Bedford, MA: Air Force Cambridge Research Laboratories, 110 p.
- Mundy, CJ, Barber, DG, Michel, C.** 2005. Variability of snow and ice thermal, physical and optical properties pertinent to sea ice algae biomass during spring. *Journal of Marine Systems* **58**: 107–120. DOI: <http://dx.doi.org/10.1016/j.jmarsys.2005.07.003>.
- Nicolaus, M, Gerland, S, Hudson, SR, Hanson, S, Haapala, J, Perovich, DK.** 2010. Seasonality of spectral albedo and transmittance as observed in the Arctic Transpolar Drift in 2007. *Journal of Geophysical Research* **115**: C11011. DOI: <http://dx.doi.org/10.1029/2009jc006074>.
- Nicolaus, M, Katlein, C, Maslanik, J, Hendricks, S.** 2012. Changes in Arctic sea ice result in increasing light transmittance and absorption. *Geophysical Research Letters* **39**: L24501. DOI: <http://dx.doi.org/10.1029/2012gl053738>.
- Painter, TH, Bryant, AC, Skiles, SM.** 2012. Radiative forcing by light absorbing impurities in snow from MODIS surface reflectance data. *Geophysical Research Letters* **39**: L17502. DOI: <http://dx.doi.org/10.1029/2012gl052457>.
- Palm, SP, Strey, ST, Spinhirne, J, Markus, T.** 2010. Influence of Arctic sea ice extent on polar cloud fraction and vertical structure and implications for regional climate. *Journal of Geophysical Research: Atmospheres* **115**: D21209. DOI: <http://dx.doi.org/10.1029/2010JD013900>.
- Palmer, MA, Saenz, BT, Arrigo, KR.** 2014. Impacts of sea ice retreat, thinning, and melt-pond proliferation on the summer phytoplankton bloom in the Chukchi Sea, Arctic Ocean. *Deep Sea Research Part II: Topical Studies in Oceanography* **105**: 85–104. DOI: <http://dx.doi.org/10.1016/j.dsr2.2014.03.016>.
- Perovich, DK.** 1996. The optical properties of sea ice. *U.S. Cold Regions Research and Engineering Laboratory Monograph*, pp. 96–1, 25, Hanover, NH.
- Perovich, DK.** 2005. On the aggregate-scale partitioning of solar radiation in Arctic sea ice during the Surface Heat Budget of the Arctic Ocean (SHEBA) field experiment. *Journal of Geophysical Research: Oceans* **110**: C3002. DOI: <http://dx.doi.org/10.1029/2004JC002512>.
- Perovich, DK, Grenfell, TC, Light, B, Hobbs, PV.** 2002. Seasonal evolution of the albedo of multiyear Arctic sea ice. *Journal of Geophysical Research* **107**(C10): 8044. DOI: <http://dx.doi.org/10.1029/2000jc000438>.
- Perovich, DK, Jones, KF, Light, B, Eicken, H, Markus, T, Stroeve, J, Lindsay, R.** 2011. Solar partitioning in a changing Arctic sea-ice cover. *Annals of Glaciology* **52**(57): 192–196. DOI: <http://dx.doi.org/10.3189/172756411795931543>.
- Perovich, DK, Nghiem, SV, Markus, T, Schweiger, A.** 2007. Seasonal evolution and interannual variability of the local solar energy absorbed by the Arctic sea ice–ocean system. *Journal of Geophysical Research* **112**(C3005). DOI: <http://dx.doi.org/10.1029/2006jc003558>.
- Perovich, DK, Polashenski, C.** 2012. Albedo evolution of seasonal Arctic sea ice. *Geophysical Research Letters* **39**: L08501. DOI: <http://dx.doi.org/10.1029/2012GL051432>.
- Platnick, S, Meyer, KG, King, MD, Wind, G, Amara-singhe, N, Marchant, B, Arnold, GT, Zhang, Z, Hubanks, PA, Holz, RE, Yang, P, Ridgway, WL & Riedi, J.** 2017. The MODIS cloud optical and microphysical products: Collection 6 updates and examples from Terra and Aqua. *IEEE Transactions on Geoscience and Remote Sensing* **55**(1): 502–525. DOI: <http://dx.doi.org/10.1109/TGRS.2016.2610522>.
- Rabbette, M, Pilewskie, P.** 2002. Principal component analysis of Arctic solar irradiance spectra. *Journal of Geophysical Research* **107**(C10): 8049. DOI: <http://dx.doi.org/10.1029/2000jc000566>.
- Renaut, S, Devred, E, Babin, M.** 2018. Northward expansion and intensification of phytoplankton growth during the early ice-free season in Arctic. *Geophysical Research Letters* **45**: 10590–10598. DOI: <http://dx.doi.org/10.1029/2018GL078995>.
- Ricchiazzi, P, Yang, S, Gautier, C, Sowle, D.** 1998. SBDART: A research and teaching software tool for plane-parallel radiative transfer in the Earth's atmosphere. *Bulletin of the American Meteorological Society* **79**(10): 2101–2114. DOI: [http://dx.doi.org/10.1175/1520-0477\(1998\)079<2101:SARATS>2.0.CO;2](http://dx.doi.org/10.1175/1520-0477(1998)079<2101:SARATS>2.0.CO;2).
- Rinke, A, Segger, B, Crewell, S, Maturilli, M, Naakka, T, Nygård, T, Vihma, T, Alshawaf, F, Dick, G, Wickert, J, Keller, J.** 2019. Trends of vertically integrated water vapor over the Arctic during 1979–2016: Consistent moistening all over? *Journal of Climate* **32**(18): 6097–6116. DOI: <http://dx.doi.org/10.1175/jcli-d-19-0092.1>.
- Sato, K, Inoue, J, Kodama, YM, Overland, JE.** 2012. Impact of Arctic sea-ice retreat on the recent change in cloud-base height during autumn. *Geophysical Research Letters* **39**(10). DOI: <https://doi.org/10.1029/2012GL051850>.

- Shupe, MD, Intrieri, JM.** 2004. Cloud radiative forcing of the Arctic surface: The influence of cloud properties, surface albedo, and solar zenith angle. *Journal of Climate* **17**(3): 616–628. DOI: [http://dx.doi.org/10.1175/1520-0442\(2004\)017<0616:CRFOTA>2.0.CO;2](http://dx.doi.org/10.1175/1520-0442(2004)017<0616:CRFOTA>2.0.CO;2).
- Slagstad, D, Wassmann, PFJ, Ellingsen, I.** 2015. Physical constrains and productivity in the future Arctic Ocean. *Frontiers in Marine Science* **2**: 85. DOI: <http://dx.doi.org/10.3389/fmars.2015.00085>.
- Stroeve, JC, Kattsov, V, Barrett, A, Serreze, M, Pavlova, T, Holland, M, Meier, WN.** 2012. Trends in Arctic sea ice extent from CMIP5, CMIP3 and observations. *Geophysical Research Letters* **39**: L16502. DOI: <http://dx.doi.org/10.1029/2012GL052676>.
- Su, W, Charlock, TP, Rose, FG, Rutan, D.** 2007. Photosynthetically active radiation from clouds and the Earth's radiant energy system (CERES) products. *Journal of Geophysical Research: Biogeosciences* **112**: G02022. DOI: <http://dx.doi.org/10.1029/2006JG000290>.
- Taskjelle, T, Granskog, MA, Pavlov, AK, Hudson, SR, Hamre, B.** 2017a. Effects of an Arctic under-ice bloom on solar radiant heating of the water column. *Journal of Geophysical Research: Oceans* **122**: 126–138. DOI: <http://dx.doi.org/10.1002/2016JC012187>.
- Taskjelle, T, Hudson, SR, Granskog, MA, Hamre, B.** 2017b. Modelling radiative transfer through ponded first-year Arctic sea ice with a plane-parallel model. *The Cryosphere* **11**: 21372148. DOI: <http://dx.doi.org/10.5194/tc-11-2137-2017>.
- Taskjelle, T, Hudson, SR, Granskog, MA, Nicolaus, M, Lei, R, Gerland, S., Stamnes, JJ, Hamre, B.** 2016. Spectral albedo and transmittance of thin young Arctic sea ice. *Journal of Geophysical Research: Oceans* **121**(1): 540–553. DOI: <http://dx.doi.org/10.1002/2015jc011254>.
- Tedesco, L, Vichi, M, Scoccimarro, E.** 2019. Sea-ice algal phenology in a warmer Arctic. *Science Advances* **5**(5): eaav4830. DOI: <http://dx.doi.org/10.1126/sciadv.aav4830>.
- Tomasi, C, Kokhanovsky, AA, Lupi, A, Ritter, C, Smirnov, A, O'Neill, NT, Stone, RS, Holben, BN, Nyeki, S, Wehrli, C, Stohl, A, Mazzola, M, Lanconelli, C, Vitale, V, Stebel, K, Aaltonen, V, Leeuw, G, Rodriguez, E, Herber, AB, Radionov, VF, Zielinski, T, Petelski, T, Sakerin, SM, Kabanov, DM, Xue, Y, Mei, L, Istomina, L, Wagener, R, McArthur, B, Sobolewski, PS, Kivi, R, Courcoux, Y, Larouche, P, Broccardo, S, Piketh, SJ.** 2015. Aerosol remote sensing in polar regions. *Earth-Science Reviews* **140**: 108–157. DOI: <http://dx.doi.org/10.1016/j.earscirev.2014.11.001>.
- Tomasi, C, Vitale, V, Lupi, A, Di Carmine, C, Campanelli, M, Herber, A, Treffeisen, R, Stone, RS, Andrews, E, Sharma, S, Radionov, V, von Hoyningen-Huene, W, Stebel, K, Hansen, GH, Myhre, CL, Wehrli, C, Aaltonen, V, Lihavainen, H, Virkkula, A, Hillamo, R, Ström, J, Toledano, C, Cachorro, VE, Ortiz, P, de Frutos, AM, Blindheim, S, Frioud, M, Gausa, M, Zielinski, T, Petelski, T, Yamanouchi, T.** 2007. Aerosols in polar regions: A historical overview based on optical depth and in situ observations. *Journal of Geophysical Research* **112**: D16205. DOI: <http://dx.doi.org/10.1029/2007jd008432>.
- Tschudi, M, Fowler, C, Maslanik, J, Stewart, JS, Meier, WN.** 2016. EASE-Grid Sea Ice Age, Version 3. Boulder, Colorado USA. NASA National Snow and Ice Data Center Distributed Active Archive Center. DOI: <http://dx.doi.org/10.5067/PFSVFZA9Y85G>.
- Wang, Q, Danilov, S, Jung, T, Kaleschke, L, Wernecke, A.** 2016. Sea ice leads in the Arctic Ocean: Model assessment, interannual variability and trends. *Geophysical Research Letters* **43**(13): 7019–7027. DOI: <http://dx.doi.org/10.1002/2016GL068696>.
- Wang, X, Key, JR.** 2003. Recent trends in Arctic surface, cloud, and radiation properties from space. *Science* **299**(5613): 1725–1728. DOI: <http://dx.doi.org/10.1126/science.1078065>.
- Yu, Y, Taylor, PC, Cai, M.** 2019. Seasonal variations of Arctic low-level clouds and its linkage to sea ice seasonal variations. *Journal of Geophysical Research: Atmospheres* **124**(22): 12206–12226. DOI: <https://doi.org/10.1029/2019JD031014>.

How to cite this article: Laliberté, J, Bélanger, S, Babin, M. 2021. Seasonal and interannual variations in the propagation of photosynthetically available radiation through the Arctic atmosphere. *Elementa: Science of the Anthropocene* 9(1). DOI: <https://doi.org/10.1525/elementa.2020.00083>

Domain Editor-in-Chief: Jody W. Deming, University of Washington, Seattle, WA, USA

Associate Editor: Lisa A. Miller, Institute of Ocean Sciences, Fisheries and Oceans Canada, Sidney, BC, Canada

Knowledge Domain: Ocean Science

Part of an Elementa Special Feature: Green Edge

Published: July 16, 2021 **Accepted:** May 27, 2021 **Submitted:** June 30, 2020

Copyright: © 2021 The Author(s). This is an open-access article distributed under the terms of the Creative Commons Attribution 4.0 International License (CC-BY 4.0), which permits unrestricted use, distribution, and reproduction in any medium, provided the original author and source are credited. See <http://creativecommons.org/licenses/by/4.0/>.



Elem Sci Anth is a peer-reviewed open access journal published by University of California Press.

OPEN ACCESS The Open Access icon, which is a stylized padlock with a circular arrow around it, indicating that the content is freely available.